metals

MDPI

Article

Strain Compensation Constitutive Model and Parameter Optimization for Nb-Contained 316LN

Jingdan Li and Jiansheng Liu *

College of Materials Science and Engineering, Taiyuan University of Science and Technology, Taiyuan 030024, China; lijingdan9@163.com

* Correspondence: b20150014@stu.tyust.edu.cn or jiansliu@163.com; Tel.: +86-133-0351-7782

Received: 13 January 2019; Accepted: 6 February 2019; Published: 12 February 2019



Abstract: Hot deformation behavior of Nb-contained 316LN was investigated using a series of compression tests performed on a Gleeble-1500D simulator at temperature of 950–1200 °C and strain rate of 0.01~1 s^{-1}. Based on the strain compensation method, a modified Arrhenius constitutive model considering the comprehensive effects of temperature, strain rate, and strain on flow stress was established, and the accuracy of the proposed model was evaluated by introducing correlation coefficient (R) and average relative error (AARE). The values of R and AARE were calculated as 0.995 and 4.48%, respectively, proving that the modified model has a high accuracy in predicting the flow stress of Nb-contained 316LN. The microstructure evolution and the dynamic recrystallization (DRX) mechanism of the experimental material were explicated by optical microscopy (OM), electron back scattered diffraction (EBSD), and transmission electron microscopy (TEM). It was found that continuous dynamic recrystallization (CDRX) characterized by subgrain evolution and discontinuous dynamic recrystallization (DDRX) featured by grain boundary nuclei are two main dynamic recrystallization (DRX) mechanisms of Nb-contained 316LN. Furthermore, based on the results of microstructure analyses, optimum parameters were obtained as temperature ranges of 1100~1200 °C and strain rate ranges of 0.01~1 s^{-1}.

Keywords: strain compensation; constitutive model; dynamic recrystallization mechanism; parameter optimization; Nb contained 316LN steel

1. Introduction

316LN is a kind of single phase austenitic stainless steel with low stacking fault energy (SFE). It is widely used in nuclear power plant components for good performance on thermal mechanical properties, corrosion resistance, irradiation resistance, and welding [1–6]. Carbide and nitride precipitation (such as $Cr_{23}C_6$, Cr_2N) during service process lead to a reduction of corrosion resistance and creep rupture ductility [7]. So Nb element is often added to stabilize C and N. Literatures [8–10] have shown that precipitation of the Z phase (a complex nitride phase), due to the addition of Nb, causes significant improvement in both creep strength and corrosion resistance of 316LN.

As the large size and complex manufacturing of nuclear power plant components, numerical simulation combined with constitutive models are usually used to predict material flow behavior under different deformation conditions. Therefore, the accuracies of constitutive models have great influences on the reliability of simulation. Constitutive models describe the relationship between flow stress and deformation parameters. In recent years, several constitutive models have been proposed, which can be classified into three types: the phenomenological based model [11–13], the physical based model [14–16], and the artificial neural network (ANN) model [17–19]. Due to high computational complexity of physical models and the requirement of a large number of training samples in ANN models, phenomenological models are widely used as the effective constitutive model. The Arrehenius

hyperbolic sine equation is a typical representative of phenomenological models. However, it only considers the effects of temperature and strain rate on flow stress and ignores the effect of strain. Lin et al. [20] proposed a modified Arrehenius constitutive model based on the compensation of strain. This model was utilized to predict the flow behavior of stainless steel [21,22], Ni-based superalloys [23,24], aluminum alloys [25], and magnesium alloys [26]. Therefore, in order to obtain an accurate constitutive model to describe the hot deformation behavior of Nb-contained 316LN, the strain compensation modified Arrehenius model was introduced in the present research.

As the strict quality requirement of nuclear power equipment, its manufacture usually adopts hot forging. During the hot forging process, the work piece undergoes changes in both shape and microstructure. It is essential to make clear the microstructure evolution mechanisms during the deformation process to obtain a desired microstructure in the component [27]. It is well known that the main softening mechanisms during hot working are dynamic recrystallization (DRX) and dynamic recovery (DRV) [28], and which softening mechanism dominates is closely related to the SFE of material [29]. For materials with high SFE, e.g., Al, Ti, and ferritic steels, DRV dominates the microstructural evolution process, and the DRX is hindered by stable dislocation substructures caused by DRV. In contrast, for materials with low SFE, e.g., Cu, Ni-based super alloys and austenitic stainless steel, dislocation cross-slip is limited, while DRX is more prevalent [30]. The SFE of Nb-contained 316LN is low, and thus DRX occurs readily during hot working. Therefore, in the current study, the DRX mechanism under various deformation conditions was investigated in detail to understand the microstructure evolution of Nb-contained 316LN.

Process parameters are the key to control the microstructure and properties of hot forged products. Unreasonable parameters result in bad mechanical properties and affect the service performance, so, it is necessary to optimize process parameters for effective production. As the manufacturing process of nuclear power plant products requires multiple heat processes and deformation paths, the stress state is complex, thus the real microstructure evolution mechanism is difficult to understand. Therefore, simple compression tests with actual manufacturing process parameters were used in the present study to investigate the microstructure evolution of Nb-contained 316LN.

In this study, hot compression tests of Nb-contained 316LN were conducted on a Gleeble-1500D thermal simulator. A strain compensation constitutive model for Nb-contained 316LN was established, and accuracy of the model was evaluated. In addition, the microstructure evolution of Nb-contained 316LN was observed by optical microscopy (OM), electron back scattered diffraction (EBSD), and transmission electron microscopy (TEM). Finally, based on the microstructure analyses, process parameters for practical manufacture were optimized.

2. Materials and Methods

Nb-contained 316LN with a chemical composition 0.027%C-16.886%Cr-12.554%Ni-2.096%Mo-1.183%Mn-0.691%Si-0.104%N-0.091%Nb-0.089%Cu-Fe was used in the current experiment. Cylindrical specimens with 8 mm in diameter and 12 mm in height were machined. Graphite flake was used to reduce the friction between the specimen's surface and tooling head.

The compression tests were carried out on a Gleeble-1500D thermal simulator (Dynamic Systems Inc., Poestenkill, NY, USA) in the temperature range of 950~1200 °C and strain rate range of 0.01~1 s^{-1}. Specimens were first heated to 1200 °C at 10 °C/s and held for 3 min, then cooled to compression temperature (950~1200 °C) at 5 °C/s, held for 1 min, and subsequently, compressed to a true strain of 0.8. Finally, the compressed samples were rapidly water quenched to keep the deformed microstructures.

Samples used for microstructure observation were taken from the deformation zone in the middle of specimens. For OM morphology, the surfaces of samples were grinded, polished to 2 μm grit diamond paste, and etched into a solution of 4 g $CuSO_4$ + 20 mL HCl + 20 mL H_2O at room temperature. The OM analysis was performed on a ZEISS-AXIO microscope (Carl Zeiss Inc., Jena, Germany). The EBSD samples were first mechanically grinded and then electrolytically polished using 10 vol PCT perchloric acid-90 vol PCT ethanol solution (Tianjin Guangcheng Chemical Reagent Co.,

Ltd., Tianjin, China) at 30 V for 30 s at room temperature. The EBSD analysis was executed on a ZEISS ULTRA 55 field-emission scanning electron microscopy (Carl Zeiss Inc., Jena, Germany) with a step size of 0.8 μm. For TEM analysis, thin foils were mechanically grinded, polished to a thickness of 50 μm and then electro-polished in a 10 vol PCT perchloric acid-90 vol PCT ethanol solution. TEM observation was carried out on a JEM F200 microscopy (JEOL Ltd., Tokyo, Japan) at 200 KV.

3. Results and Discussion

3.1. Hot Compression Deformation Behaviors

The true strain-true stress curves of Nb-contained 316LN at different deformation conditions are shown in Figure 1. It is noticeable that at different strains, the flow stress of curves show different characteristics. At the initial stage of deformation (with a small strain), the flow stress increased rapidly due to the rapid increase of dislocation density (caused by work hardening) in the material. Then, the increase speed of flow stress slowed down due to the softening effect of DRV. But the value of flow stress still increased because work hardening effect was far greater than the softening effect caused by DRV. As the strain continued to accumulate, the flow stress began to decrease and reached a steady stress state because the stored deformation energy was enough to accelerate DRX, which could consume dislocations by forming new recrystallized grains. It can be found that the ultimate shape of curves are determined by the competition between work hardening and DRX. At strain rate of 1 s^{-1}, except for the curve of 1200 °C, all of the other curves were seen to be plateau-shaped, while at strain rates of 0.01 s^{-1} and 0.1 s^{-1}, all of the curves first reached a peak value and then descended to a platform.

Further, it can be seen that the flow stresses of curves are sensitive to the deformation temperature and strain rate. Flow stress decreased with the increasing temperature and the decreasing strain rate. This is because at a certain strain rate, higher deformation temperatures resulted in greater dislocation activity, which could promote the nucleation and growth of DRX and reduce the value of flow stress. Moreover, when the deformation temperature was constant, there was enough time to complete the softening effect caused by DRX at lower strain rates, thus leading to the decrease in flow stress.

Therefore, it is essential to consider the comprehensive effects of strain, strain rate, and temperature on flow stress in the development of the constitutive model for Nb-contained 316LN.

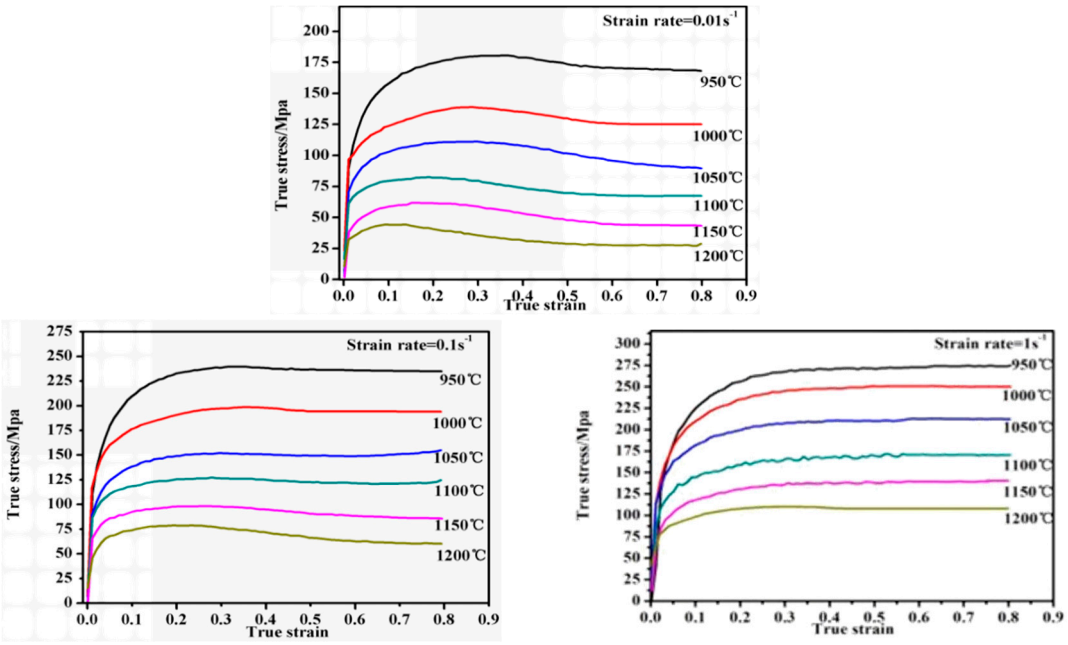


Figure 1. True strain-true stress curves of Nb-contained 316LN.

3.2. Constitutive Model

3.2.1. Determination of Material Constants for the Constitutive Model

The Arrhenius equations are widely used to describe the relationship among flow stress, strain rate, and temperature; the equations can be expressed as [31]:

$$\dot{\varepsilon} = A\prime\sigma^{n\prime} \qquad \text{for } \alpha\sigma < 0.8, \tag{1}$$

$$\dot{\varepsilon} = A'' \exp(\beta\sigma) \qquad \text{for } \alpha\sigma > 1.2, \tag{2}$$

$$\dot{\varepsilon} = A[\sinh(\alpha\sigma)]^{n} \exp(-Q/RT) \quad \text{for all } \sigma, \tag{3}$$

where $\dot{\varepsilon}$ is the strain rate (s^{-1}), σ is the flow stress (MPa), $A\prime$, A'', A, β, α, $n\prime$ and n are material constants, Q is the deformation activation energy (KJ/mol), R is the universal gas constant (8.314 J/(mol·K)), T is absolute temperature (K). In principle, the temperature of the work piece will rise due to adiabatic heating during deformation, especially at higher strain rates ($\geq 1\ s^{-1}$). But in the present research, the effect of aidabatic heating on flow stress was not considered.

For the determination of A'', A, β, α, $n\prime$, n and Q, the Zener-Hollomon parameter [32] was introduced:

$$Z = \dot{\varepsilon} \exp(Q/RT), \tag{4}$$

A true strain of 0.1, as an example, was used to express the solution process of the material constants and Q. First, taking the logarithm of both sides of Equations (1) and (2), Equations (5) and (6) could be obtained. Then, the constant $n\prime$, β were calculated through the mean slope of six lines in $\ln\sigma - \ln\dot{\varepsilon}$ and $\sigma - \ln\dot{\varepsilon}$ plots as shown in Figure 2a,b. Based on $\alpha = \beta/n$, the value of α at strain 0.1 was calculated as 0.0083.

$$\ln\dot{\varepsilon} = \ln A\prime + n\prime \ln\sigma, \tag{5}$$

$$\ln\dot{\varepsilon} = \ln A'' + \beta\sigma, \tag{6}$$

Taking the logarithm of both sides of Equation (3), as shown below:

$$\ln[\sinh(\alpha\sigma)] = \frac{1}{n}\ln\dot{\varepsilon} - \frac{1}{n}\ln A + \frac{Q}{nRT}, \tag{7}$$

According to the Equation (7), the constant n and Q were obtained, respectively, through the mean slope of lines in $\ln[\sinh(\alpha\sigma)] - \ln\dot{\varepsilon}$ and $\ln[\sinh(\alpha\sigma)] - 1/T$ plots, as shown in Figure 2c,d.

By substituting Equation (4) to Equation (3), the Equation (8) could be obtained:

$$Z = \dot{\varepsilon}\exp(\frac{Q}{RT}) = A[\sinh(\alpha\sigma)]^{n}, \tag{8}$$

Then, taking the logarithm of both sides of Equation (8), as shown below:

$$\ln Z = \ln A + n\ln[\sinh(\alpha\sigma)], \tag{9}$$

The constant A could be calculated through the intercept of the line in $\ln Z - \ln[\sinh(\alpha\sigma)]$ plot, as shown in Figure 3.

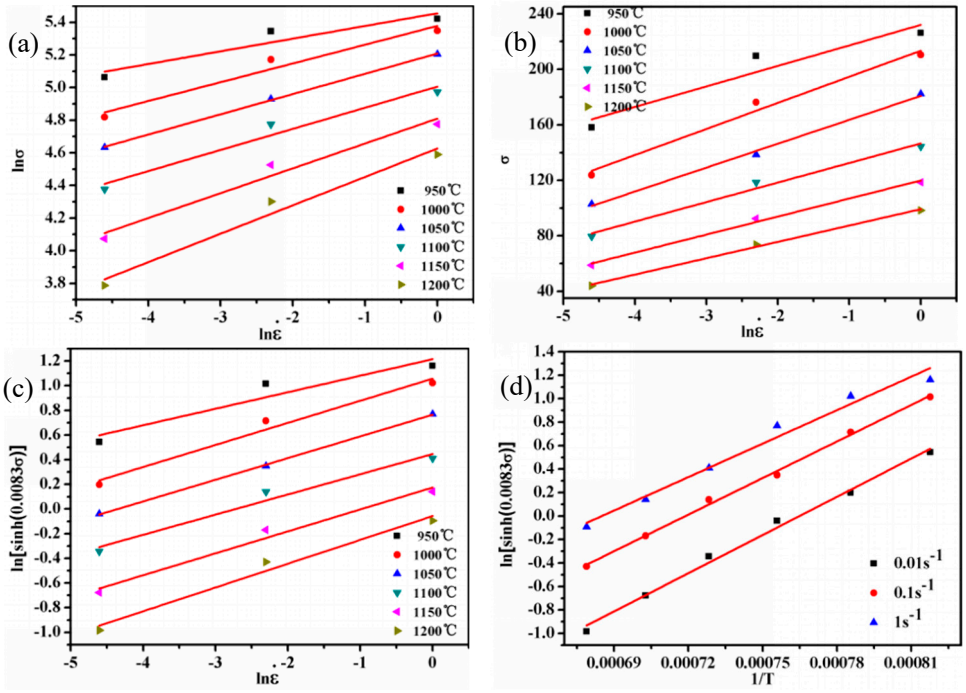


Figure 2. Linear relationship fitting (**a**) $\ln\sigma - \ln\dot{\varepsilon}$, (**b**) $\sigma - \ln\dot{\varepsilon}$, (**c**) $\ln[\sinh(\alpha\sigma)] - \ln\dot{\varepsilon}$, (**d**) $\ln[\sinh(\alpha\sigma)] - 1/\mathrm{T}$.

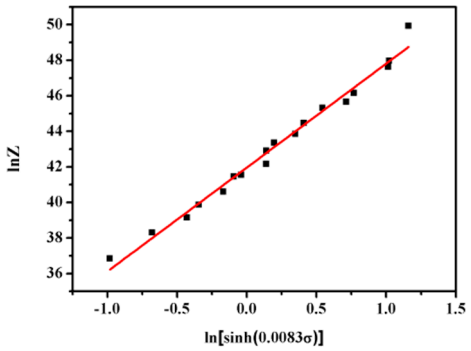


Figure 3. Linear relationship between ln$Z$ and ln[sinh(ασ)].

3.2.2. Constitutive Model Base on Strain Compensation

Through the analysis of Section 3.1, it can be seen that strain has a great influence on flow stress of Nb-contained 316LN steel, so the strain compensation method was adopted in order to obtain an accurate material constitutive model. Based on the strain compensation theory proposed by Lin et al. [20], the effect of strain on flow stress is mainly reflected in material constants of the model. Hence, the values of material constants α, n, ln$A$ and Q in the strain range of 0.1~0.8 with an interval of 0.1 were solved by the same means in Section 3.2.1. It can be seen from Table 1, the effect of strain on material parameters is significant. The relationships between material constants and strains are shown in Equation (10). Fifth order polynomials were used to fit each parameter. It is discernible from Figure 4 that the values of linear correlation coefficients because all curves are greater than 0.95.

$$\begin{cases} \alpha = 0.00985 - 0.0208\varepsilon + 0.06027\varepsilon^2 - 0.0663\varepsilon^3 + 0.02214\varepsilon^4 + 0.00321\varepsilon^5 \\ n = 6.95 - 14.36\varepsilon + 58.05\varepsilon^2 - 152.13\varepsilon^3 + 184.76\varepsilon^4 - 80.77\varepsilon^5 \\ Q = 557.64 - 876.29\varepsilon + 5025.17\varepsilon^2 - 14234.59\varepsilon^3 + 17424.76\varepsilon^4 - 7630.16\varepsilon^5 \\ \ln A = 49.252 - 130.085\varepsilon + 748.57\varepsilon^2 - 2003.28\varepsilon^3 + 2365.46\varepsilon^4 - 1015.44\varepsilon^5 \end{cases} \quad (10)$$

Table 1. Constitutive equation parameters under different true strains.

Material Constants	0.1	0.2	0.3	0.4	0.5	0.6	0.7	0.8
α	0.0083	0.0076	0.0074	0.0075	0.0077	0.0078	0.0079	0.0079
n	5.96	5.45	5.06	4.66	4.28	4.04	3.94	3.93
Q (KJ/mol)	507.661	495.109	485.028	468.141	447.376	430.784	425.602	421.504
ln$A$	41.96	40.57	40.286	38.86	37.06	35.61	35.12	34.74

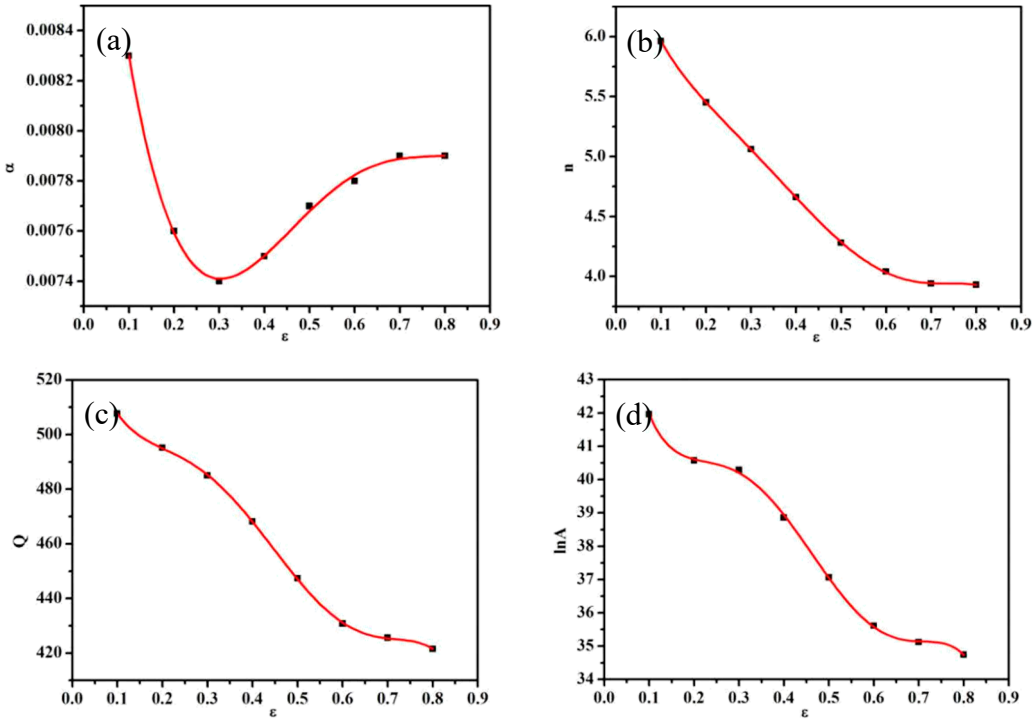


Figure 4. The relationship between equation parameters and true strain: (**a**) α, (**b**) n, (**c**) Q, (**d**) ln$A$.

3.2.3. Verification

According to Equations (3) and (4), the flow stress can be expressed as below:

$$\sigma = (1/\alpha) \ln \left\{ \left[(Z/A)^{2/n} + 1 \right]^{1/2} + (Z/A)^{1/n} \right\} \tag{11}$$

Since the values of α, n, ln$A$ and Q at various strain could be calculated by Equation (10), the flow stress of the strain compensation constitutive model of Nb-contained 316LN at different conditions was obtained by substituting these material constants, temperature, and strain rate into Equation (11). Figure 5 shows the comparison between experimental flow stresses and predicted flow stresses calculated by the strain compensation constitutive model. It is evident that the predicted flow stress values are in good agreement with the experimental ones. In order to evaluate the accuracy of the proposed model, correlation coefficient R and average absolute relative error AARE [33] were introduced as shown in Equations (12) and (13).

$$R = \frac{\sum_{i=1}^{N} (\sigma_e^i - \overline{\sigma}_e)(\sigma_p^i - \overline{\sigma}_p)}{\sqrt{\sum_{i=1}^{N} (\sigma_e^i - \overline{\sigma}_e)^2 \sum_{i=1}^{N} (\sigma_p^i - \overline{\sigma}_p)^2}} \tag{12}$$

$$AARE = \frac{1}{N}\sum_{i=1}^{N}\left|\frac{\sigma_e^i - \sigma_p^i}{\sigma_e^i}\right| \times 100\% \quad (13)$$

where σ_e is the real flow stress value obtained from compression experiment, σ_p is the predicted flow stress value based on the strain compensation constitutive model. $\overline{\sigma}_e$ is the average value of σ_e, $\overline{\sigma}_p$ is the average value of σ_p, N is the total amount of data.

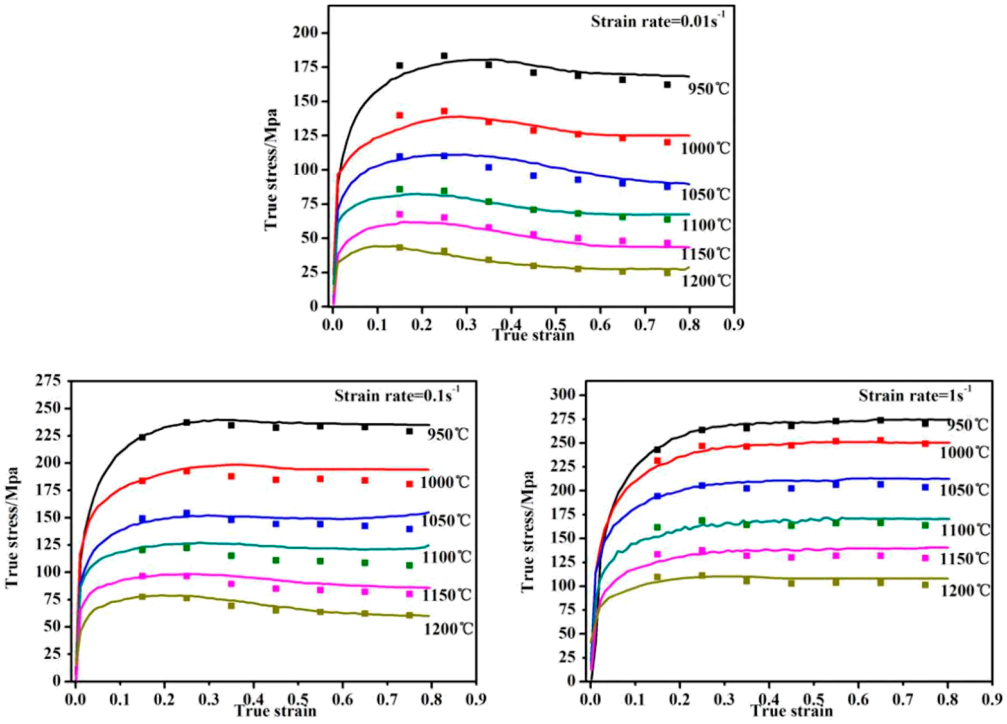


Figure 5. Comparison between predicted and experimental flow stress curves.

As shown in Figure 6, the values of correlation coefficient R and average relative error AARE were calculated as 0.996 and 3.75%, respectively, demonstrating that the proposed strain compensation constitutive model has high accuracy and reliability in predicting the flow stress of Nb-contained 316LN.

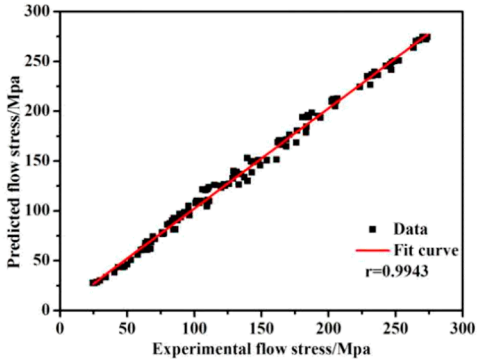


Figure 6. Relationship between predicted flow stress and experimental flow stress.

3.3. Microstructure Evolution

The original metallographic picture of Nb-contained 316LN used in this paper is shown in Figure 7. The average grain size was measured as 180 μm. Annealing twins with straight grain boundaries existed in the microstructure. For Nb-contained 316LN is a kind of Face Center Cubic structure stainless steel with low SFE, the occurrence of twins is frequent.

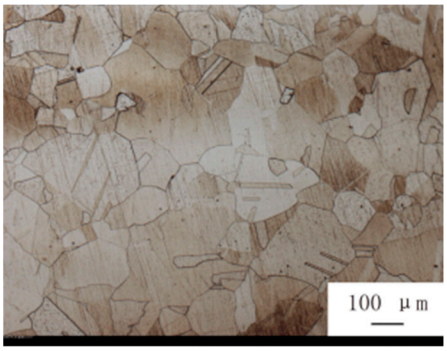


Figure 7. Original morphology of Nb-contained 316LN.

Typical microstructures of the specimens after hot compression are displayed in Figure 8, and it can be found that the recrystallized fraction and grain size are increased with increasing temperature and decreasing strain rate. Based on the morphology differences observed by OM, the microstructure of compressed specimens could be classified into four groups. In group 1, a large number of original grains were severely elongated, small recrystallized grains began to form, and cluster around the original grain boundary, and the recrystallization fraction was very low (Figure 8a,d). In group 2, the recrystallized fraction increased significantly compared to group 1 where newly formed recrystallized grains replaced the original microstructures; however, a small number of elongated non-recrystallized original grains still existed in the microstructures (Figure 8b,e,g). In group 3, the recrystallization was almost complete, uniform equiaxed recrystallized grain composed the microstructures (Figure 8c,f,h). In group 4, the recrystallized grains became coarser, abnormal grain growth occurred in the microstructure (Figure 8i).

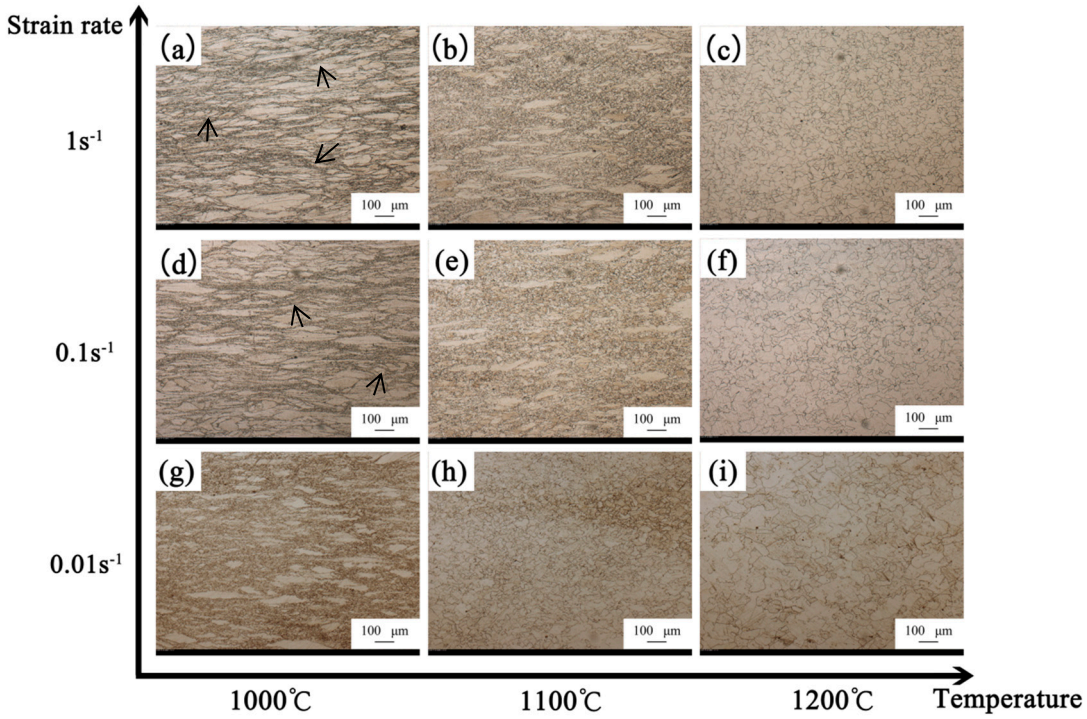


Figure 8. Effects of temperature and strain rate on microstructure of Nb-contained 316LN at strain of 0.8.

Based on the analysis above, it can be concluded that the morphology of the specimen after hot compression is decided by the DRX, so it is essential to make clear the DRX mechanism of Nb-contained 316LN. EBSD tests were conducted on the specimens after compressed under these four groups' conditions, typical microstructures are shown in Figure 9. Figure 9a represents the microstructure of group 1 that was compressed at 1000 °C and 1 s^{-1}. It is observable that the microstructure was

composed of both large size deformed original grain with dense low angle boundary (high density dislocations) and newly formed dislocation free grains. According to the EBSD analysis program "Recrystallized Fraction Component", the recrystallized grain could be clarified with different color, the recrystallized fraction could be measured. Combining with the EBSD analysis program "Grain Statistics", the average size of recrystallized grains could be determined. EBSD analysis data shows that the recrystallized fraction of Figure 9a is only 22%, average size of the recrystallized grains is 3.6 μm, the microstructure is very inhomogeneous. Moreover, serrated original grain boundaries surrounded with small size recrystallized grains (black arrows show) indicate that the discontinuous dynamic recrystallization (DDRX) is a kind of DRX mechanism of specimens compressed under conditions of group 1. In addition, segments of high angle boundary (blue arrows show) appeared in the interior of deformed grains indicate that the continuous dynamic recrystallization (CDRX) is another DRX mechanism of specimens compressed under conditions of group 1. It is worth noting that unlike the DDRX grains are formed by boundary bulging nucleation, the CDRX grains are considered as a result of subgrain evolution. To get better insight of the CDRX mechanism of Nb-contained 316LN, the TEM analysis was performed on the thin foil taken from the deformation zone in the middle of the sample compressed at 1100 °C and 0.1 s^{-1} and the corresponding TEM micrographs are shown in Figure 10. It is discernible that due to hot deformation, plenty of dislocations were produced in the original grain, and consequently, dislocations began to rearrange and formed subgrain boundaries as shown in Figure 10a. Then, the misorientation angle of subgrain boundary increased by absorbing dislocations as shown in Figure 10b. Eventually, with the misorientation angle of subgrain boundary transformed from low to high, newly formed dislocation free grains started to replace the original grain.

Figure 9b represents the microstructure of group 2 that was compressed at 1100 °C and 0.1 s^{-1}. The obtained EBSD data express that the recrystallized fraction is 72%, average size of recrystallized grains is 22.5 μm. Although the microstructure became uniform comparing to group 1, some unrecrystallized areas with low angle boundaries still existed. Arrows signed in Figure 9b show the evidence of bulging nuclei and subgrain evolution, indicating that CDRX and DDRX are two main DRX mechanisms of specimens compressed at conditions of group 2.

Figure 9c is a typical microstructure of group 3 that was compressed at 1200 °C and 1 s^{-1}. The microstructure consisted of uniform dislocation free recrystallized grains with an average size of 32.5 μm and the recrystallized fraction was measured as 95%. This indicates that DRX was well carried out under conditions of group 3 and DRX played an important role in grain refinement. Moreover, Figure 9c exhibits that the recrystallized grain boundaries are composed by Σ3 (60° misorientation around <111>) boundaries.

Figure 9d shows the microstructure of group 4 that was compressed at 1200 °C and 0.01 s^{-1}. Abnormal grain growth indicates that complete DRX finished at the initiation of compression and there was enough time for recrystallized grain growth at 1200 °C and 0.01 s^{-1}. In addition, it can be seen that some low angle boundaries were distributed in the interior of coarsen grain. This is because deformation still imposed on the specimen during recrystallized grain growth, and dislocations were produced in the grown up recrystallized grain.

Although microstructure characteristic of group 3 and group 4 were observed, the DRX mechanism of these two groups cannot be seen intuitively. So microstructures of specimens compressed under a smaller strain at the same temperature and strain rate as those of group 3 and group 4 were observed as shown in Figure 11. From Figure 11a, it can be seen that at temperature 1200 °C, strain rate 1 s^{-1}, and strain 0.2, DRX just initiated. Serrated grain boundary and newly formed recrystallized grain along the original boundaries indicate the occurrence of DDRX (shown by black arrows). In addition, some newly formed recrystallized grain (marked by blue arrows) existed in the interior of original grain, indicating that CDRX is another DRX mechanism in the sample. Figure 11b is the microstructure of specimen compressed under strain 0.2 at 1200 °C and 0.01 s^{-1}. It is discernible that the original grain was completely replaced by grown up recrystallized grains, thus demonstrating that DRX occurred adequately at a small strain when temperature is 1200 °C and strain rate is 0.01 s^{-1}. This happened

because the high temperature of 1200 °C accelerated the activity of dislocation and the low strain rate of 0.01 s^{-1} afforded enough time for dislocation movement. It is also obvious that DDRX and CDRX are two main DRX mechanisms at conditions of group 4.

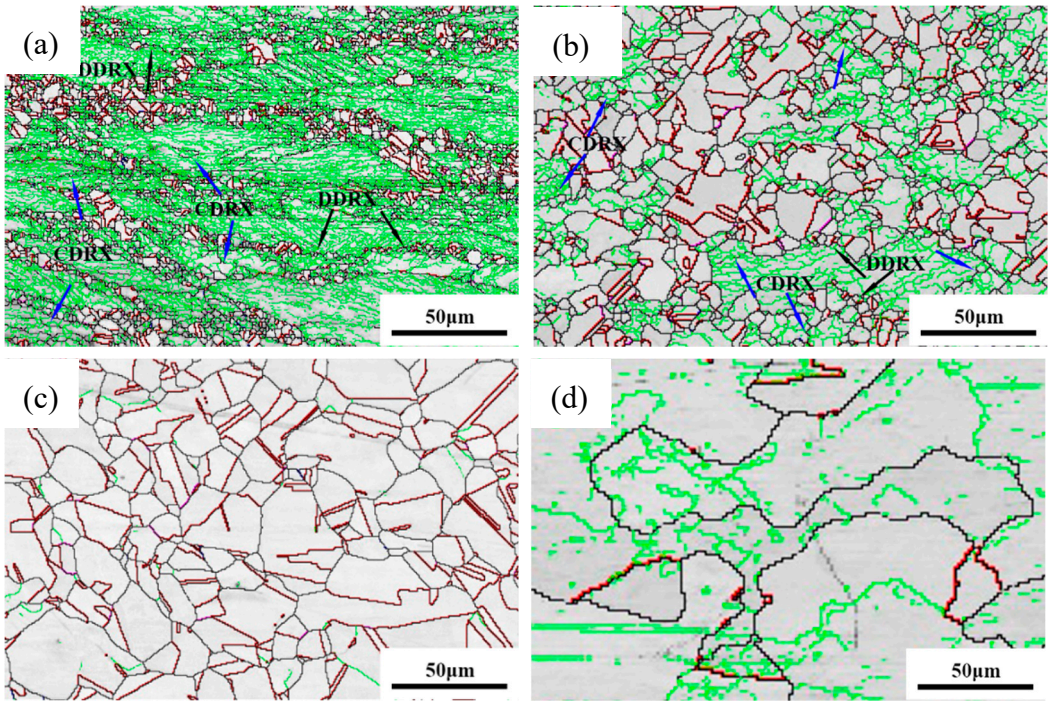


Figure 9. EBSD grain boundary maps of compressed samples (**a**) 1000 °C, 1 s^{-1} (**b**) 1100 °C, 0.1 s^{-1} (**c**) 1200 °C, 1 s^{-1} (**d**) 1200 °C, 0.01 s^{-1} (2–15° green, Σ3 red, Σ9 purple, Σ11 yellow, Σ27 aqua and other boundaries black).

It is clear from the above analysis that the DRX mechanisms of Nb-contained 316LN are DDRX and CDRX, and the microstructure evolution of Nb-contained 316LN is sensitive to the change of deformation parameters. The recrystallization fraction was low and microstructure inhomogeneity was serious in the samples compressed under temperature 1000 °C with strain rate ≥0.1 s^{-1}. Moreover, as arrows shown in Figure 8a,d, flow localization appeared in the microstructure of samples, so these parameters should be avoided during the formulation of process parameters. A higher DRX fraction and finer grain size were obtained in the microstructure of samples compressed at 1000 °C with a strain rate of 0.01 s^{-1} and at 1100 °C with strain rates ≥0.1 s^{-1}, implying that the parameters in above mentioned range is feasible for the formulation of process parameters; however, some unrecrystallized grain still existed in the microstructures. The microstructures of the samples compressed at 1100 °C with a strain rate of 0.01 s^{-1} and at 1200 °C with strain rates ≥0.1 s^{-1} were fine and uniform, so, the optimum parameters should be chosen in this range. However, the microstructure of the sample compressed at 1200 °C with a strain rate of 0.01 s^{-1} was composed of coarse grains, and thus these parameters should be avoided due to the harmful mechanical properties caused by coarse grains.

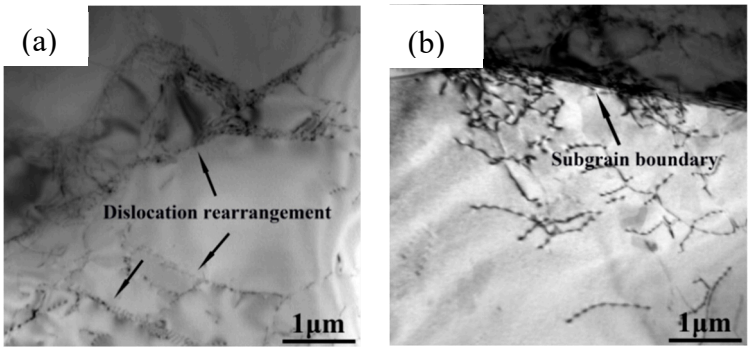


Figure 10. TEM micrographs of the Nb-contained 316LN compressed at 1100 °C, 0.1 s^{-1} (**a**) dislocation rearrangement (**b**) subgrain boundary transformation.

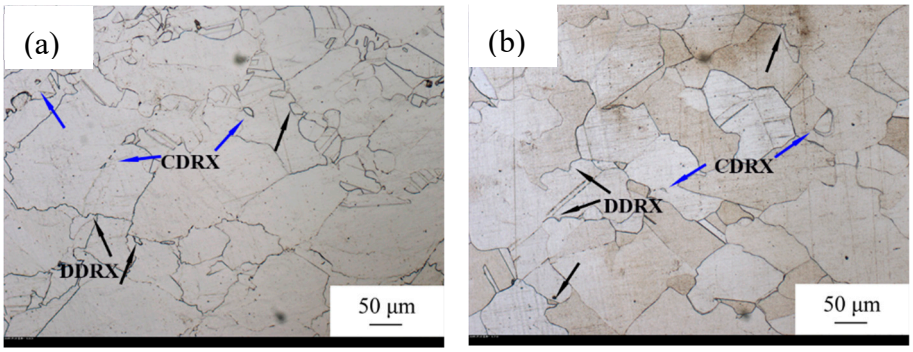


Figure 11. OM maps of Nb-contained 316LN compressed under strain 0.2 and at (**a**) 1200 °C, 1 s^{-1} (**b**) 1200 °C, 0.01 s^{-1}.

4. Conclusions

Hot deformation behavior of Nb-contained 316LN steel was investigated in this paper. A strain compensation constitutive model was established to describe the flow behavior of Nb-contained 316LN steel. Microstructure evolution mechanism of Nb-contained 316LN compressed under various conditions was discussed. Practical manufacture parameters were optimized. The conclusions can be drawn as follows:

(1) A strain compensation constitutive model of Nb-contained 316LN was developed. The relationship between material constants and true strain was fitted by fifth order polynomial. The comparison between the predicted flow stress and the experimental flow stress indicates that the proposed model possesses high accuracy and reliability to predict the hot deformation behavior of Nb-contained 316LN.

(2) DDRX characterized by grain boundary bulging nuclei and CDRX characterized by subgrain evolution are two main DRX mechanisms during the hot deformation of Nb-contained 316LN.

(3) Parameters were optimized based on the results of microstructure analyses. Parameters with temperature $\leq$1000 °C, strain rate $\geq$0.1 s^{-1} and temperature $\geq$1200 °C, strain rate $\leq$0.01 s^{-1} should be avoided. The optimum processing parameters should be chosen in the temperature range of 1100~1200 °C and strain rate range of 0.01~1 s^{-1}.

Author Contributions: J.L. (Jingdan Li) and J.L. (Jiansheng Liu) conceived and designed the experiments; J.L. (Jingdan Li) performed the experiments, analyzed the data and wrote the paper; J.L. (Jiansheng Liu) provided guidance and all sorts of support during the work.

Funding: This work is financially supported by the National Natural Science Foundation of China (No. 51775361).

Conflicts of Interest: The authors declare no conflict of interest.

References

1. Kim, D.W.; Chang, J.H.; Ryu, W.S. Evaluation of the creep-fatigue damage mechanism of type 316L and type 316LN stainless steel. *Int. J. Pres. Ves. Pip.* **2008**, *85*, 378–384. [CrossRef]
2. Li, X.Q.; Zhao, J.J.; Xu, J.C.; Liu, X. Mechanical Properties and Defective Effects of 316LN Stainless Steel by First-Principles Simulations. *J. Mater. Sci. Technol.* **2011**, *27*, 1029–1033. [CrossRef]
3. Ganesh Kumar, J.; Ganesan, V.; Laha, K.; Mathew, M.D. Time dependent design curves for a high nitrogen grade of 316LN stainless steel for fast reactor applications. *Nucl. Eng. Des.* **2013**, *265*, 949–956. [CrossRef]
4. Xiao, W.K.; Zhu, L.; Zhang, F.J.; Dai, K.S.; Zai, X.; Yang, X.; Chen, B.J. Effect of heat input on cryogenic toughness of 316LN austenitic stainless steel NG-MAG welding joints with large thickness. *Mater. Des.* **2015**, *86*, 160–167.
5. Dai, K.S.; He, P.; Zhu, L.; Zhang, F.J.; Chen, F.Y.; Zhai, X.; Xiao, W.K. Effect of solution treatment on microstructure and cryogenic toughness of 316LN austenite stainless steel weld metal welded by NG-MAG arc welding. *Fusion Eng. Des.* **2017**, *125*, 178–188. [CrossRef]
6. Xu, D.M.; Li, G.Q.; Wan, X.L.; Xiong, R.L.; Xu, G.; Wu, K.M.; Somani, M.C.; Misra, R.D.K. Deformation behavior of high yield strength—High ductility ultrafine-grained 316LN austenitic stainless steel. *Mater. Sci. Eng. A* **2017**, *688*, 407–415. [CrossRef]
7. Kim, D.W. Influence of nitrogen-induced grain refinement on mechanical properties of nitrogen alloyed type 316LN stainless steel. *J. Nucl. Mater.* **2012**, *420*, 473–478. [CrossRef]
8. Vodárek, V. Creep behaviour and microstructural evolution in AISI 316LN + Nb steels at 650 °C. *Mater. Sci. Eng. A* **2011**, *528*, 4232–4238. [CrossRef]
9. Perron, A.; Toffolon-Masclet, C.; Ledoux, X.; Buy, F.; Guilbert, T.; Urvoy, S.; Bosonnet, S.; Marini, B.; Cortial, F.; Tecier, G.; et al. Understanding sigma-phase precipitation in a stabilized austenitic stainless steel (316Nb) through complementary CALPHAD-based and experimental investigations. *Acta Mater.* **2014**, *79*, 16–29. [CrossRef]
10. Lu, W.J.; Hua, X.Z.; Zhou, X.L.; Huang, J.H.; Peng, X.Y. Aging precipitation behaviors of Nb-contained 316LN SS. *J. Alloy. Compd.* **2017**, *701*, 993–1002. [CrossRef]
11. Lin, Y.C.; Ding, Y.; Chen, M.S.; Deng, J. A new phenomenological constitutive model for hot tensile deformation behaviors of a typical Al–Cu–Mg alloy. *Mater. Des.* **2013**, *52*, 118–127. [CrossRef]
12. EI Mehtedi, M.; Gabrielli, F.; Spigarelli, S. Hot workability in process modeling of a bearing steel by using combined constitutive equations and dynamic material model. *Mater. Des.* **2014**, *53*, 398–404. [CrossRef]
13. Lin, Y.C.; Li, L.T.; Jiang, Y.Q. A Phenomenological Constitutive Model for Describing Thermo-Viscoplastic Behavior of Al-Zn-Mg-Cu Alloy Under Hot Working Condition. *Exp. Mech.* **2012**, *52*, 993–1002. [CrossRef]
14. Vilamosa, V.; Clausen, A.H.; Børvik, T.; Holmedal, B.; Hopperstad, O.S. A physically-based constitutive model applied to AA6082 aluminium alloy at large strains, high strain rates and elevated temperatures. *Mater. Des.* **2016**, *103*, 391–405. [CrossRef]
15. Bobbili, R.; Ramudu, B.V.; Madhu, V. A physically-based constitutive model for hot deformation of Ti-10-2-3 alloy. *J. Alloys Compd.* **2017**, *696*, 295–303. [CrossRef]
16. Dong, D.Q.; Chen, F.; Cui, Z.S. A physically-based constitutive model for SA508-III steel: Modeling and experimental verification. *Mater. Sci. Eng. A* **2015**, *634*, 103–115. [CrossRef]
17. Guo, L.F.; Li, B.C.; Zhang, Z.M. Constitutive relationship model of TC21 alloy based on artificial neural network. *Trans. Nonferrous Met. Soc. China* **2013**, *23*, 1761–1765. [CrossRef]
18. He, A.; Wang, X.T.; Xie, G.L.; Yang, X.Y.; Zhang, H.L. Modified Arrhenius-type Constitutive Model and Artificial Neural Network-based Model for Constitutive Relationship of 316LN Stainless Steel during Hot Deformation. *J. Iron Steel Res. Int.* **2015**, *22*, 721–729. [CrossRef]
19. Rezaei Ashtiani, H.R.; Shahsavari, P. A comparative study on the phenomenological and artificial neural network models to predict hot deformation behavior of AlCuMgPb alloy. *J. Alloys Compd.* **2016**, *687*, 263–273. [CrossRef]
20. Lin, Y.C.; Chen, M.S.; Zhong, J. Constitutive modeling for elevated temperature flow behavior of 42CrMo steel. *Comput. Mater. Sci.* **2008**, *42*, 470–477. [CrossRef]
21. Cao, Y.; Di, H.S.; Misra, R.D.K.; Yi, X.; Zhang, J.C.; Ma, T.J. On the hot deformation behavior of AISI 420 stainless steel based on constitutive analysis and CSL model. *Mater. Sci. Eng. A* **2014**, *593*, 111–119. [CrossRef]

22. Pu, E.X.; Feng, H.; Liu, M.; Zheng, W.; Dong, H.; Song, Z. Constitutive Modeling for Flow Behaviors of Superaustenitic Stainless Steel S32654 during Hot Deformation. *J. Iron Steel Res. Int.* **2016**, *23*, 178–184. [CrossRef]
23. Tan, Y.B.; Ma, Y.H.; Zhao, F. Hot deformation behavior and constitutive modeling of fine grained Inconel 718 superalloy. *J. Alloys Compd.* **2018**, *741*, 85–96. [CrossRef]
24. Lin, Y.C.; Nong, F.Q.; Chen, X.M.; Chen, D.D.; Chen, M.S. Microstructural evolution and constitutive models to predict hot deformation behaviors of a nickel-based superalloy. *Vacuum* **2017**, *137*, 104–114. [CrossRef]
25. Li, J.; Li, F.G.; Cai, J.; Wang, R.T.; Yuan, Z.W.; Ji, G.L. Comparative investigation on the modified Zerilli-Armstrong model and Arrhenius-type model to predict the elevated-temperature flow behaviour of 7050 aluminium alloy. *Comput. Mater. Sci.* **2013**, *71*, 56–65. [CrossRef]
26. Changizian, P.; Zarei-Hanzak, A.; Ali, A.R. The high temperature flow behavior modeling of AZ81 magnesium alloy considering strain effects. *Mater. Des.* **2012**, *39*, 384–389. [CrossRef]
27. Mandal, S.; Bhadur, A.K.; Sarma, V.S. Role of twinning on dynamic recrystallization and microstructure during moderate to high strain rate hot deformation of a Ti-Modified austenitic stainless steel. *Metall. Mater. Trans. A* **2012**, *43*, 2056–2068. [CrossRef]
28. Saboori, A.; Dadkhah, M.; Pavese, M.; Manfredi, D.; Biamino, S. Hot deformation behavior of Zr-1%Nb alloy: Flow curve analysis and microstructure observations. *Mater. Sci. Eng. A* **2017**, *696*, 366–373. [CrossRef]
29. Allain, S.; Chateau, J.P.; Bouaziz, O.; Migot, S.; Guelton, N. Correlations between the calculated stacking fault energy and the plasticity mechanisms in Fe–Mn–C alloys. *Mater. Sci. Eng. A* **2004**, *387–389*, 158–162. [CrossRef]
30. Mataya, M.C.; Nilsson, E.R.; Brown, E.L.; Krauss, G. Hot working and recrystallization of as-cast 317L. *Metall. Mater. Trans. A* **2003**, *34*, 3021–3041. [CrossRef]
31. Sellars, C.M.; McTegart, W.J. On the mechanism of hot deformation. *Acta Metall.* **1966**, *14*, 1136–1138. [CrossRef]
32. Zener, C.; Hollomon, J.H. Effect of Strain Rate Upon Plastic Flow of Steel. *J. App. Phys.* **1944**, *15*, 22–32. [CrossRef]
33. Liao, C.; Wu, H.; Wu, C.; Zhu, F.; Lee, S. Hot deformation behavior and flow stress modeling of annealed AZ61 Mg alloys. *Prog. Natl. Sci. Mater. Int.* **2014**, *24*, 253–265. [CrossRef]



© 2019 by the authors. Licensee MDPI, Basel, Switzerland. This article is an open access article distributed under the terms and conditions of the Creative Commons Attribution (CC BY) license (http://creativecommons.org/licenses/by/4.0/).